Direct numerical simulation of conical shock wave/turbulent boundary layer interaction

Feng-Yuan Zuo[1,2]†, Antonio Memmolo[2], Guo-ping Huang[1], and Sergio Pirozzoli[2]‡

[1]College of Energy and Power Engineering, Nanjing University of Aeronautics and Astronautics, Nanjing, 210016, China

[2]Sapienza Università di Roma, Dipartimento di Meccanica e Aerospaziale, Via Eudossiana 18, 00184 Roma, Italy

Direct numerical simulation of the Navier-Stokes equations is carried out to investigate the interaction of a conical shock wave with a turbulent boundary layer developing over a flat plate at free-stream Mach number $M_\infty = 2.05$ and Reynolds number $Re_\theta \approx 630$, based on the upstream boundary layer momentum thickness. The shock is generated by a circular cone with half opening angle $\theta_c = 25°$. As found in experiments, the wall pressure exhibits a distinctive N-wave signature, with a sharp peak right past the precursor shock generated at the cone apex, followed by an extended zone with favourable pressure gradient, and terminated by the trailing shock associated with recompression in the wake of the cone. The boundary layer behavior is strongly affected by the imposed pressure gradient. Streaks are suppressed in adverse pressure (APG) zones, but reform rapidly in downstream favorable pressure gradient (FPG) zones. Three-dimensional mean flow separation is only observed in the first APG region associated with formation of a horseshoe vortex, whereas the second APG region features an incipient detachment state, with scattered spots of instantaneous reversed flow. As found in canonical geometrically two-dimensional wedge-generated shock/boundary layer interactions, different amplification of the turbulent stress components is observed through the interacting shock system, with approach to isotropic state in APG regions, and to a two-component anisotropic state in FPG. General adequacy of Boussinesq hypothesis is found to predict the spatial organization of the turbulent shear stresses, although different eddy viscosities should be used for each component, as in tensor eddy-viscosity models, or in full Reynolds stress closures.

Key words: conical shock waves, compressible boundary layers, turbulence, DNS

1. Introduction

Shock wave/turbulent boundary layer interactions (SBLI) occur whenever a shock sweeps across the boundary layer developing on a wall surface, and as a consequence they have great interest in aeronautics and aerospace engineering. SBLIs are found in several situations of practical importance, such as wing-fuselage and tail-fuselage junctions of an aircraft, helicopter blades, supersonic intakes, over-expanded nozzles,

† Email address for correspondence: zuofy@nuaa.edu.cn
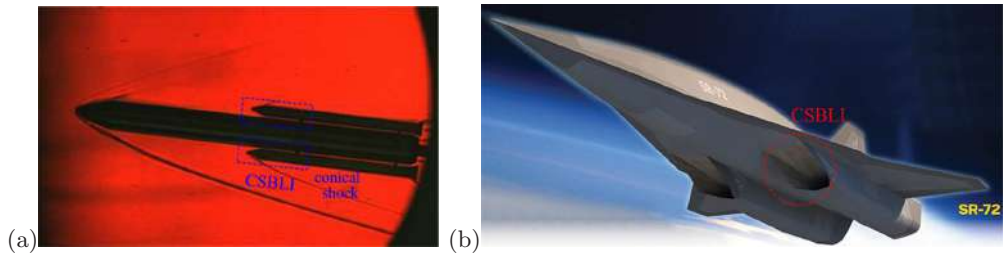‡ Email address for correspondence: sergio.pirozzoli@uniroma1.it

Figure 1. Conical SBLI in launch vehicle during the ascent phase (a) and in the air intake of the hypersonic SR-72 vehicle (b).

launch vehicles during the ascent phase, etc. Typically, these phenomena have a significant drawback on aerodynamic performance, yielding loss of efficiency of aerodynamic surfaces, unwanted wall pressure fluctuations possibly leading to vibration and fatigue of structural components, and to localized heat transfer loads, especially in presence of flow separation (Dolling 2001; Smits & Dussauge 2006; Babinsky & Harvey 2011). A large number of experimental and numerical studies, along with the concurrent development of flow control techniques, have been carried out in past decades, but nevertheless the unsteady features and the turbulence amplification mechanisms conveyed by SBLI are not fully understood, remaining a challenging state-of-the-art research problem.

Most studies of SBLI have been carried out in idealized settings involving geometrically two-dimensional configurations, and/or using simplified modeling approaches (Délery. & Dussauge 2009; DeBonis *et al.* 2012; Morgan *et al.* 2013). As a common conclusion, these investigations have proved that turbulence models have the ability to capture the mean flow features such as the pressure loads and the interaction length scales, but obviously they cannot capture the unsteady features and correctly predict flow separation. The most relevant studies on SBLI in geometrically two-dimensional configurations have been carried out experimentally or numerically through high-fidelity simulations (Adams 2000; Pirozzoli & Grasso 2006; Smits & Dussauge 2006; Dupont *et al.* 2006; Pirozzoli & Bernardini 2011*a*; Touber & Sandham 2011; Hadjadj 2012). The overall picture involves a boundary layer which develops under APG conditions, with the effects of the shock that are felt upstream of the impingement as a result of propagation of information in the subsonic part of the boundary layer. In case the shock is strong enough, separation takes place and pressure shows a plateau in the separation region, with a typical low-frequency motion of the shock system and of the separation bubble. Turbulence experiences amplification while traversing the shock, and it undergoes a relaxation process as is proceeds past the interaction region. However, SBLI occurring in flow conditions of practical relevance are almost invariably three-dimensional in nature. Most often, shock waves are generated by finite-sized bodies, and interact with turbulent boundary layers developing on solid surfaces. Conical shocks in particular are frequently found in high-speed vehicles, both in external and internal flows, for which examples are provided in figure 1. In the supersonic ascent phase, multi-body launch vehicles feature conical shock boundary layer interactions (CSBLI) associated with reflection of the boosters-generated shocks with the main body of the launcher (see panel a, from (Sziroczak & Smith 2016)). CSBLI also occur in internal flows as in the hypersonic wave-catcher (inward-turning) intake adopted on the SR-72 vehicle (Zuo *et al.* 2016; Zuo & Huang 2018), sketched in panel (b). As shown in figure 2, the initially conical shock wave covers the intake edge, and it reflects as another conical shock impinging on the upper surface.
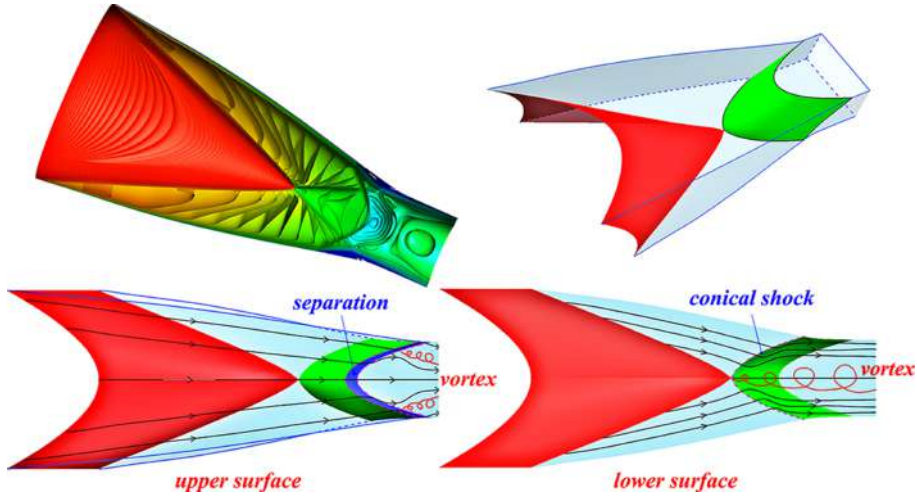
FIGURE 2. Sketch of flow structure in wave-catcher inward-turning intake (Zuo & Huang 2018). Red and green surfaces are conical shocks, the purple surface is the separation region, red lines are a sketch of vortices caused by CSBLI.
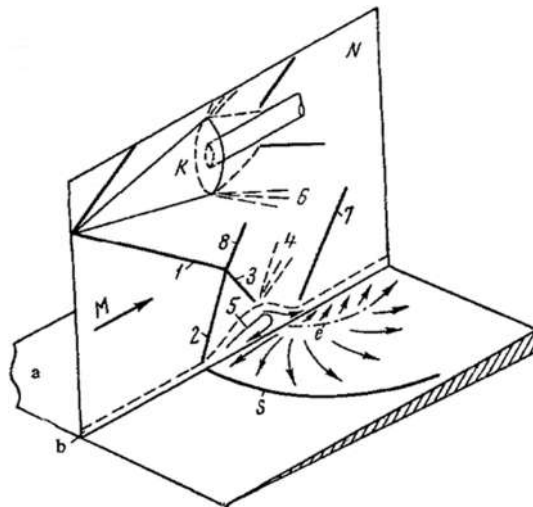

FIGURE 3. Flow-field structure of strong CSBLI under separation condition (Panov 1968). Numbered solid lines are conical shock traces; numbered dashed lines are rarefaction waves; 5 is the separation region, delimited in the wall plane by S (separation) and e (reattachment).

The analysis of CSBLI is inherently more difficult than for planar SBLI, in that the flow field past a conical shock is not uniform, and the wall pressure rise is not uniform along the boundary-layer transverse direction, hence the resulting limiting wall streamlines are not parallel. Moreover, non-uniformity of the imposed shear yields a variety of complex vortical structures which interact and merge while becoming entrained in the main flow. Greater challenge is also encountered in the numerical simulation of CSBLI, mainly because of slow convergence of the flow statistics in the absence of directions with spatial homogeneity. The leading features of CSBLI are sketched in figure 3, taken from Panov (1968). The shock generator K generates the incident conical shock 1, and 2 is the three-dimensional separation shock associated with separation of the boundary layer. The approaching flow that passes through shock 2 is deflected upward, and after passing

through shock 3 and rarefaction wave 4, the separated boundary layer is directed at some angle toward the plate surface. Shock 7 then arises to realign the outer flow to the wall-parallel direction. The boundary layer, which separates along line S (coalescence line), reattaches along line e (divergence line). As in the case of the later analysis, the rarefaction wave 6 emanating from the trailing edge of the shock-generating device can also enter into play thus further complicating the analysis of the flow in the interaction region. The overall phenomenon, with special reference to the separation region 5 is inherently three-dimensional in nature.

A mathematical analysis of CSBLI was carried out by Migotsky & Morkovin (1951). One of the main conclusions was that, even when regular reflection is possible at the leading edge of the interaction zone, transition to Mach reflection shall occur somewhere along the spanwise direction. Gai & Teh (2000) experimentally investigated the interaction of the shock wave produced by a conical shock with a planar turbulent boundary layer, at free-stream Mach number 2. By varying the cone opening angles from 14° to 30°, both attached and separated conditions were achieved. The results showed that the incident shock imposes a significant pressure gradient in the spanwise direction yielding strong cross flow and formation of a horseshoe vortex whose signature was evident in surface oil-flow visualizations, and whose size and strength gradually reduce away from the symmetry plane. Notably, the pressure rise for incipient separation was found to be less than for the geometrically two-dimensional case. Hale (2015) studied the impingement of a conical shock wave on a plane turbulent boundary layer at Mach number 2.05, and gathered informations by means of surface oil flow, pressure-sensitive paint and particle image velocimetry techniques. The experimental data suggested that the interaction causes locally two-dimensional separation near the centerline, and three-dimensional separation away from this region, with fluid propagating away from the centerline. Significant spanwise and streamwise expansion was observed right downstream of the interaction leading edge, unlike in equivalent geometrically two-dimensional wedge-generated SBLI. The results further gave hints for instantaneous boundary layer separation, and showed that the interaction tends to suppress large-scale vortical structures in the incoming boundary layer.

Based on the survey of the state-of-the-art in CSBLI we believe that further study is appropriate. In particular, we find that limited information about the detailed three-dimensional structure of the interaction has been gained through experiments, and no high-fidelity computation (i.e. LES and/or DNS) has been reported so far. Hence, we believe that a DNS-based analysis of CSBLI can help the research community in achieving improved physical understanding of the phenomenon, and to developed better turbulence models for simplified predictions. To make our analysis sufficiently general, we consider a relatively simple geometrical set-up, whereby a fully developed turbulent boundary layer progresses on a flat solid surface, and the shock wave generated by a circular cone with axis parallel to the wall is made to interact with it, mimicking the experimental flow conditions of Hale (2015). The paper is organized as follows. The numerical methodology is described in §2; the results are presented in §3, covering a quantitative analysis of the mean and statistical properties of the flow field. Concluding remarks are given in §4.

2. Computational strategy

We solve the three-dimensional Navier-Stokes equations for a perfect Newtonian gas. The molecular viscosity μ is assumed to obey Sutherland's law, and the thermal conductivity k is related to μ through $k = c_p \mu / \mathrm{Pr}$, where the molecular Prandtl number Pr is assumed to be 0.72. The Cartesian solver used for the present analysis was
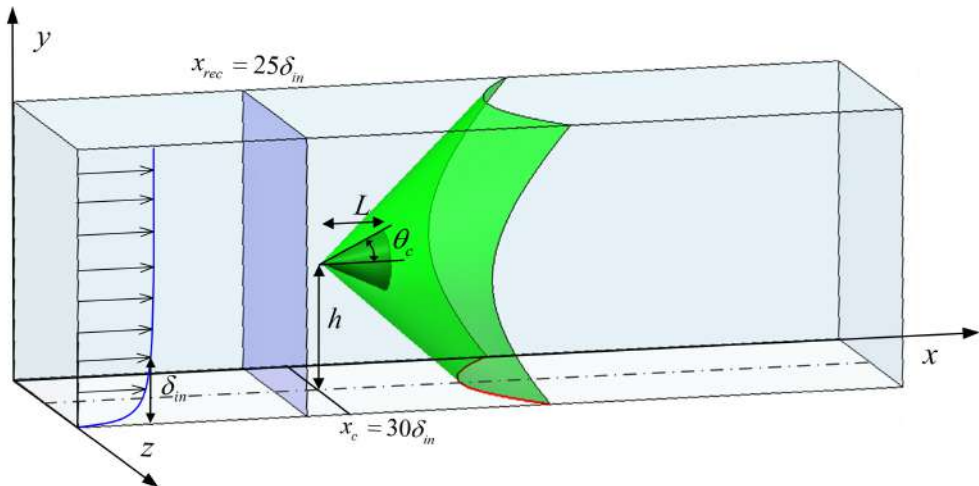
FIGURE 4. Sketch of computational domain for CSBLI analysis. δ_{in} is the inflow boundary layer thickness, x_{rec} is the boundary layer recycling station, x_c is the x coordinate of the cone leading edge. The green surface depicts the conical shock, whose wall trace is highlighted in red.

extensively tested for compressible wall-bounded flows, also in presence of impinging shocks (Pirozzoli *et al.* 2010; Pirozzoli & Bernardini 2011*a*). The main feature of the solver is the use of a conservative discretization of the convective fluxes which combines sixth-order central non-dissipative discretization in smooth parts of the flow field and seventh-order weighted-essentially non-oscillatory (WENO) discretization in shocked regions, the switch between the two being controlled by a shock sensor based on the ratio of local dilatation to vorticity modulus (Pirozzoli 2011). For the purpose of hybridization, critical grid nodes are first marked and then padded with four nodes on both sides to ensure that the stencil of the underlying non-dissipative scheme does not cross shocked zones. Improved numerical stability for the central discretization in smooth parts of the flow is achieved by splitting the convective derivatives as (Pirozzoli 2010)

$$\frac{\partial \rho u_j \varphi}{\partial x_j} = \frac{1}{4} \frac{\partial \rho u_j \varphi}{\partial x_j} + \frac{1}{4} \left(u_j \frac{\partial \rho \varphi}{\partial x_j} + \rho \frac{\partial u_j \varphi}{\partial x_j} + \varphi \frac{\partial \rho u_j}{\partial x_j} \right) + \frac{1}{4} \left(\rho u_j \frac{\partial \varphi}{\partial x_j} + \rho \varphi \frac{\partial u_j}{\partial x_j} + u_j \varphi \frac{\partial \rho}{\partial x_j} \right),$$
(2.1)

where φ stands for a generic transported fluid property. The continuous derivative operators are then replaced with central finite difference approximations using a locally conservative formulation (Pirozzoli 2010), which guarantees global conservation of mass, momentum, and total energy through the telescopic property and simplifies hybridization with the WENO algorithm. An important property of the convective split form (2.1) is that it leads to kinetic energy preservation for inviscid, incompressible flow, guaranteeing strong numerical stability without reverting to upwinding or filtering. The diffusive terms in the Navier-Stokes equations are also approximated with sixth-order central differences after being expanded to Laplacian form to guarantee finite molecular dissipation at all resolved wavelengths. Time advancement is performed by means of a standard three-stage third-order explicit Runge-Kutta algorithm.

2.1. *Computational domain*

The computational domain employed for the simulation is sketched in figure 4. The choice of the streamwise extent ($L_x = 150\delta_{in}$, with δ_{in} the inflow boundary layer thickness) is dictated by the requirement of having a sufficient boundary layer development
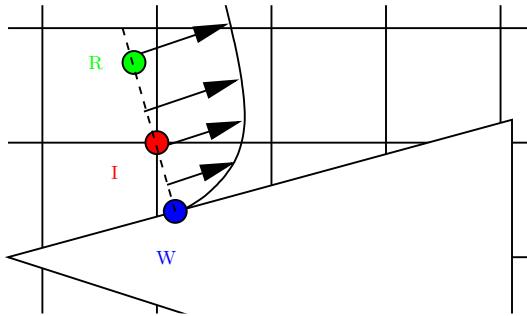
FIGURE 5. Sketch of the immersed-boundary treatment. I is the interface node, and W and R are the corresponding wall-normal foot and reflected control point.

region past the inflow and to analyze the recovery region past the interacting shock. The spanwise length ($L_z = 60\delta_{in}$) guarantees that no spurious coherence develops in the upstream boundary layer, and allows to minimize numerical blocking from the side boundaries. The domain height ($L_y = 30\delta_{in}$) is such that numerical wave reflections from the upper boundary are also minimized. Based on previous experience with DNS of SBLI and of a set of preliminary simulations, the domain has been discretized with a grid including $1536 \times 384 \times 1280$ nodes. Uniform spacing is used in the streamwise and spanwise directions, whereas nodes are clustered in the wall-normal (y) direction according to a hyperbolic sine stretching function up to $y/\delta_{in} = 6.5$. In terms of wall units evaluated in the undisturbed boundary layer upstream of the interaction zone, the streamwise and spanwise spacings are $\Delta x^+ \approx 10$, $\Delta z^+ \approx 5$, respectively, whereas the spacing in the wall-normal direction ranges between 0.7 at the wall and 12. Here and elsewhere, the $+$ subscript is used to denote normalization with respect to the friction velocity $u_\tau = \sqrt{\tau_w/\rho_w}$ (where τ_w and ρ_w are the wall shear stress and density), and the viscous length scale $\delta_v = \nu_w/u_\tau$ (where ν_w is the wall kinematic viscosity). As a further a-posteriori check, we have computed the local Kolmogorov length scale according to $\eta = (\overline{\nu}^3/\varepsilon)^{1/4}$, with the isotropic dissipation rate estimated from

$$\varepsilon = 2\overline{\nu} \left(\widetilde{S_{ij}''S_{ij}''} - \frac{1}{3}\widetilde{\frac{\partial u_k''}{\partial x_k}\frac{\partial u_l''}{\partial x_l}} \right) . \qquad (2.2)$$

We have found that the effective grid spacing $\Delta = (\Delta x \Delta y \Delta z)^{1/3}$ is nowhere larger than about three local Kolmogorov length scales, which is more than sufficient for DNS. Velocity and pressure spectra were also analyzed, and shown to yield no spurious energy pile-up at the smallest resolved wavenumbers.

2.2. *Treatment of shock generator*

In order to accommodate the conical shock generator in the Cartesian mesh used for the DNS we rely on the immersed boundary method, using the direct forcing approach of Fadlun *et al.* (2000), in which the Navier-Stokes equations are replaced by suitable interpolation formulas at the interface nodes between solid and fluid. A geometrical preprocessor based on the ray tracing algorithm (O'Rourke 1998) is applied to tag solid and fluid nodes. Once the fluid nodes are located, we identify the subset of nodes for which discretization of the Navier-Stokes equations involves the use of solid nodes, which are tagged as interface nodes and used to indirectly prescribe desired values to the conservative variables conditions at the fluid/body interface. For that purpose (see

figure 5), for each interface node (I) a wall-normal line is considered, along which a control point (R) is considered, at fixed distance from the wall foot (W), where the flow variables are interpolated from neighboring grid nodes. An equilibrium wall function is then used to define the flow variables at I based on those at R (Tessicini *et al.* 2002). Implementation details are provided in Bernardini *et al.* (2016). The cone is resolved with approximately 72, 56 and 138 grid intervals in the streamwise, wall-normal and spanwise directions, respectively, and the distance of the reflected control points from the nearest wall expressed in local wall units along the cone ranges between 3 and 70. We believe that, although the boundary layer on the cone is certainly not well resolved, this is not a major shortcoming, as the cone simply serves as a disturbing element to force a spatially varying pressure gradient onto the underlying boundary layer. Validity of the approach is confirmed by later comparison with experiments.

2.3. *Flow conditions*

The flow conditions are selected to be as close as possible to the reference experiment of Hale (2015). The shock is generated by a circular cone with height $L/\delta_{in} = 6.835$ and half opening angle is $\theta_c = 25°$. The apex of the cone is at $x_c = 30\delta_{in}$, and its axis is parallel to the wall at a distance $h/\delta_{in} = 13.67$ (see figure 4). The upstream flow has Mach number $M_\infty = 2.05$, and the Reynolds number based on the inflow boundary layer thickness is $Re_{\delta_{in}} = 5000$. The latter is about a factor of fifty less than the reference experiment, but as will be shown later this is not the cause of major quantitative differences.

A critical issue in the numerical simulations of spatially developing flows is the prescription of suitable inflow conditions to achieve a fully developed boundary layer state within the shortest possible fetch. In the present DNS this is achieved through a rescaling-recycling procedure (Xu & Martin 2004), whereby a cross-stream slice of the flow field is extracted at every Runge-Kutta sub-step at the recycling station x_{rec}, and fed back to the inflow upon suitable rescaling. This approach generates a realistic turbulent boundary layer within a short distance from the inflow, and it allows to control skin friction and thickness of the simulated boundary layer. To minimize spurious time periodicity that may result from application of quasi-periodic boundary conditions in the streamwise direction, the recycling station is set at $x_{rec} = 25\delta_{in}$, also sufficiently upstream of the cone apex. Non-reflecting characteristic boundary conditions are applied to the outflow, at the top boundary, and in the spanwise direction for $x > x_{rec}$, whereas spanwise periodicity is assumed for $x \leqslant x_{rec}$. Unsteady characteristic boundary conditions are specified at the bottom no-slip wall (Poinsot & Lele 1992), with temperature set to its adiabatic value. Flow statistics have been collected from time $t_0 u_\infty/\delta_{in} \approx 216$ to time $t_f u_\infty/\delta_{in} \approx 1572$, at intervals of $\Delta t u_\infty/\delta_{in} \approx 0.1$. The long sampling time is needed to achieve convergence of point-wise statistics in time in the absence of homogeneous directions, and it makes the present calculation quite time-consuming. The statistical analysis is carried out by splitting the instantaneous quantities into their mean and fluctuating components, using either the standard Reynolds decomposition ($f = \overline{f} + f'$) or the density-weighted (Favre) decomposition ($f = \widetilde{f} + f''$), where $\widetilde{f} = \overline{\rho f}/\overline{\rho}$.

3. Results

3.1. *Characterization of the incoming boundary layer*

A necessary check is that the incoming boundary layer is properly developed prior to interaction with the conical shock. For that purpose, we consider a reference station at $x_{ref} = 27.5\delta_{in}$, located upstream of the cone leading edge. The global boundary-layer

	M_e	Re_θ	Re_{δ_2}	Re_τ	C_f	δ^*/δ	θ/δ	H	H_i
DNS	2.05	630	410	160	3.63×10^{-3}	0.326	0.082	3.97	1.60
Hale (2015)	2.05	31900	20810	4490	1.53×10^{-3}	–	–	–	1.33

TABLE 1. Properties of incoming turbulent boundary layer at the reference station $x_{ref} = 27.5\delta_{in}$. $M_e = u_e/c_e$; $Re_\theta = \rho_e u_e \theta/\mu_e$; $Re_{\delta_2} = \rho_e u_e \theta/\mu_w$; $Re_\tau = \rho_w u_\tau \delta/\mu_w$; $C_f = 2\tau_w/(\rho_e u_e^2)$; $H = \delta^*/\theta$; $H_i = \delta_i^*/\theta_i$. The subscript e denotes properties evaluated at the edge of the boundary layer.
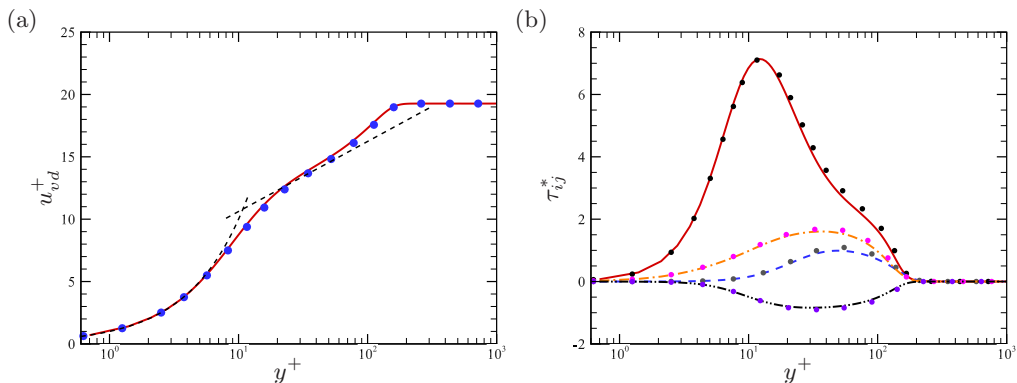

FIGURE 6. Van Driest transformed mean streamwise velocity (a), and density-scaled turbulent stresses (b) at the reference station ($x_{ref} = 27.5\delta_{in}$). Lines refer to the present DNS data, and symbols to reference data (Pirozzoli & Bernardini 2011b) at $M_\infty = 2$. In panel (a) the dashed line denotes a compound of $u^+ = y^+$ and $u^+ = 5.0 + 1/0.41 \log y^+$. In panel (b) we show τ_{11}^* (solid), τ_{22}^* (dashed); τ_{33}^* (dash-dot); τ_{12}^* (dash-dot-dot).

properties at this station are listed in table 1, where δ is the 99% thickness, δ^* is the displacement thickness,

$$\delta^* = \int_0^{\delta_e} \left(1 - \frac{\bar\rho}{\rho_e}\frac{\bar u}{u_e}\right) \mathrm{d}y, \qquad (3.1)$$

and θ is the momentum thickness,

$$\theta = \int_0^{\delta_e} \frac{\bar\rho}{\rho_e}\frac{\bar u}{u_e}\left(1 - \frac{\bar u}{u_e}\right)\mathrm{d}y, \qquad (3.2)$$

the upper integration limit δ_e denoting the edge of the rotational part of the boundary layer, defined as the point where the mean spanwise vorticity becomes less than $0.005u_\infty/\delta_{in}$ (Pirozzoli *et al.* 2010). The subscript e is used to denote the corresponding external flow properties. The table also reports equivalent incompressible boundary layer properties evaluated by setting to unity the density ratios in equations (3.1), (3.2), and referred to with the subscript i. Table 1 also shows the same parameters for the reference experiment of Hale (2015), which has much higher Reynolds number.

The van Driest effective velocity,

$$u_{vd} = \int_0^{\bar u} \left(\frac{\bar\rho}{\bar\rho_w}\right)^{1/2} d\bar u, \qquad (3.3)$$

is used in figure 6a to compare with boundary layer data at very similar flow conditions (Pirozzoli & Bernardini 2011b), with minor difference in Mach number. The same solver was used, and the only relevant difference in the computational setup was the location of the recycling station, which was set at $x_{rec} = 50\delta_{in}$. Comparison with the reference data is quite good, and in particular the velocity profiles show linear behavior up to $y^+ \simeq 5$, as expected for adiabatic boundary layers (Smits & Dussauge 2006), and a narrow range with near logarithmic variation. Comparison of the density-scaled velocity correlations

$$\tau_{ij}^* = \frac{\overline{\rho \widetilde{u_i'' u_j''}}}{\tau_w}, \tag{3.4}$$

is also shown in figure 6b. The agreement with the reference data is again quite good, which leads us to conclude that the upstream boundary layer well corresponds to a healthy state of equilibrium wall turbulence.

3.2. *General flow organization*

Having established the properties of the incoming boundary layer, we proceed to describe the main features of the flow upon interaction with the conical shock. For that purpose time-averaged and instantaneous fields of density, pressure and streamwise velocity are shown in the symmetry plane in figure 7. The flow exhibits an overall organization similar to experimental observations (Hale 2015), with the shock wave generated by the cone which impinges on the bottom wall surface, thus leading to CSBLI. This is clearly seen in density field, which well highlights the overall wave pattern. The main interacting shock is generated as straight at the cone surface, and subsequently it bends backward upon merging with the expansion fan which arises at the cone trailing edge. A continuous compression may be inferred from the pressure contours along the cone surface, which may be justified recalling that the flow is not uniform past conical shocks, unlike for planar shocks. The shock impinges on the bottom wall at $x/\delta_{in} \approx 45$. The streamwise velocity contours in figure 7e well highlights the thickening of the boundary layer in this region. As also in canonical planar interactions (Pirozzoli & Grasso 2006), the reflected wave system consists of a precursor wave associated with the upstream influence mechanism, and a trailing wave associated with boundary layer reattachment. The figures also bring out the presence of an extended low-speed region in the wake of the cone with turbulent flow, which is closed by a conical recompression shock (Herrin & Dutton 1994), originating at $x/\delta_{in} \approx 50$, and interacting with the developing boundary layer at $x/\delta_{in} \approx 75$. An additional weak compression wave is also seen to be generated at the upper boundary of the computational domain owing to imperfect radiation of numerical disturbances, and hitting the wall at $x/\delta_{in} \approx 100$. The dynamical character of the reflected shock system, which oscillates back and forth may be clearly appreciated in an attached supplementary movie.

To understand the three-dimensional character of the flow field, wall-normal/streamwise sections at two additional spanwise locations are reported in figure 8, where instantaneous density contours are plotted using the same style as in figure 7. The figure shows that the conical shock traces are not straight lines as in the symmetry plane, but rather they have hyperbolic shape, as should be the case. Additional features should be also noted. In particular, we find that reflection of the primary interaction shock changes from regular to Mach type (Migotsky & Morkovin 1951). Second, the density jump across the shock decreases gradually owing to flow three-dimensionality and interaction of the expansion fan originating at the cone trailing edge. Third, the wake recompression shock has a similar structure as the primary conical shock, and its in-wall trace is also hyperbolic.
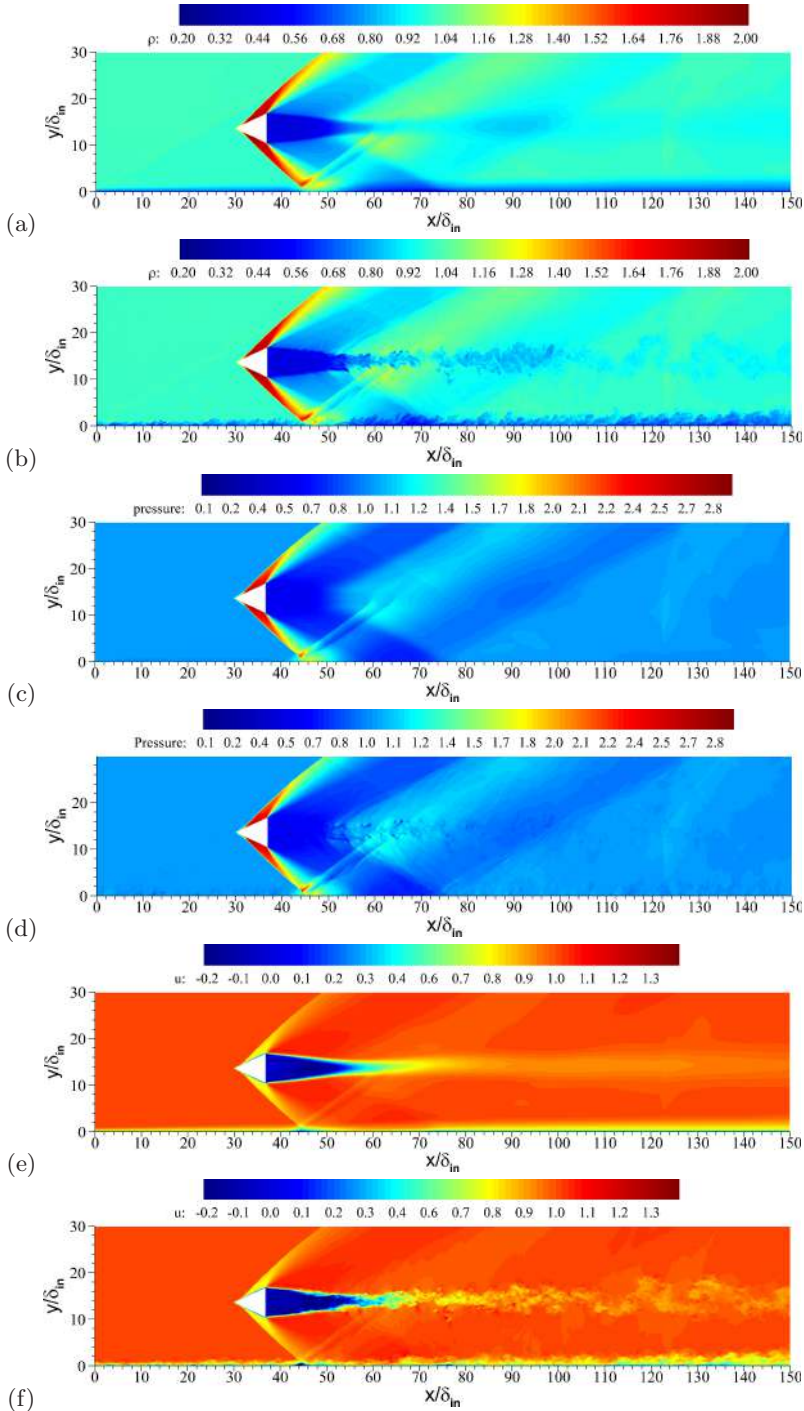
FIGURE 7. Visualization of time-averaged (a, c, e) and instantaneous (b, d, f) flow field in the symmetry plane ($z = 0$). The blank region corresponds to the conical shock generator. Panels (a, b): density, $0.2 \leqslant \bar{\rho}/\rho_\infty \leqslant 2.0$; panels (c, d): pressure, $0.1 \leqslant \bar{p}/p_\infty \leqslant 2.9$; panels (e, f): streamwise velocity, $-0.2 \leqslant \bar{u}/u_\infty \leqslant 1.4$. Color scale from blue to red.
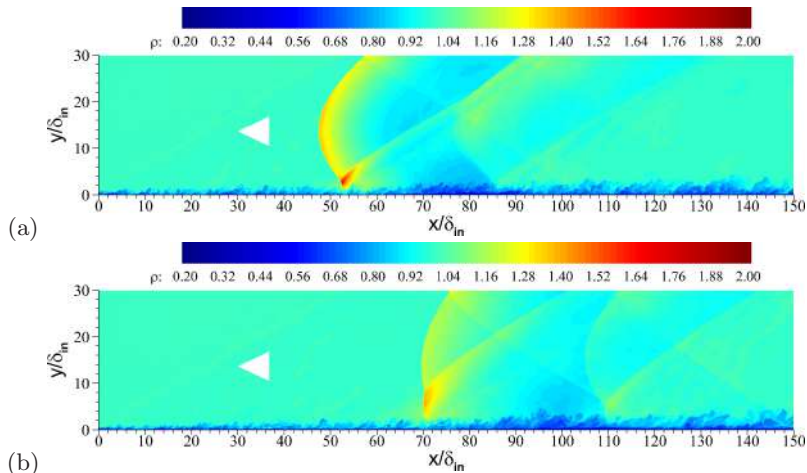
FIGURE 8. Instantaneous density contours at $z/\delta_{in} = -15$ (a), $z/\delta_{in} = -30$ (b). Contours are shown for $0.2 \leqslant \rho/\rho_\infty \leqslant 2.0$, from blue to red. The cone trace in the symmetry plane is shown for reference purposes.

Migotsky & Morkovin (1951) theoretically analyzed the reflection of a conical shock from a planar surface in the limit of strictly inviscid flow. They predicted that transition from regular to Mach reflection should occur at a critical value of the angle formed by the normal to the shock trace in the wall plane with the streamwise direction (φ, see figure 9b). At the flow conditions under scrutiny here, transition should occur for $\varphi \approx 9°$. In order to visualize the shock structure in the present DNS, in figure 9 we show contours of the shock sensor. Information is also provided in figure 9 in a series of planes normal to the shock wall trace. To clarify the occurrence of different types of shock reflection, in panels (d-f) we show contours of the thermodynamic entropy ($s = p/\rho^\gamma$), with superimposed the estimated boundary layer edge (solid blue line) and the mean sonic line (black dashed line), as a lower boundary for shock existence. The analysis is here complicated by the presence of the boundary layer, which is itself the cause of substantial increase of entropy from the free stream toward the wall, and which causes refraction of the shock wave as it penetrates layers with lower speed, masking the possible occurrence of triple points inside the boundary layer. Outside the boundary layer, the reflection type is easily classified upon inspection of the thermodynamic entropy in the neighbourhood of the candidate triple point, which is higher for fluid crossing the normal shock foot as compared to fluid crossing the two oblique shocks. Based on the available data, we may conclude that reflection is likely to be of regular type for control planes 1 and 2, whereas it is certainly of Mach type starting at control plane 3, for which a distinct triple point emerges outside the boundary layer. Accordingly, higher entropy is observed for fluid particles traveling underneath the triple point than above.

A three-dimensional rendering of the flow structures is provided in figure 10, which includes iso-surfaces of pressure, streamwise velocity contours in a near-wall plane, and pressure contours in a side plane. This figure qualitatively brings out the strong relationship between the shock system and the boundary layer evolution, also observed in planar shock interactions (Aubard *et al.* 2013; Pirozzoli & Bernardini 2011*a*). Specifically, figure 10 shows the presence of elongated streaks of high- and low-speed momentum in the ZPG region. As the boundary layer penetrates the first APG region it experiences strong retardation, and a region of low momentum forms past the upstream branch of the
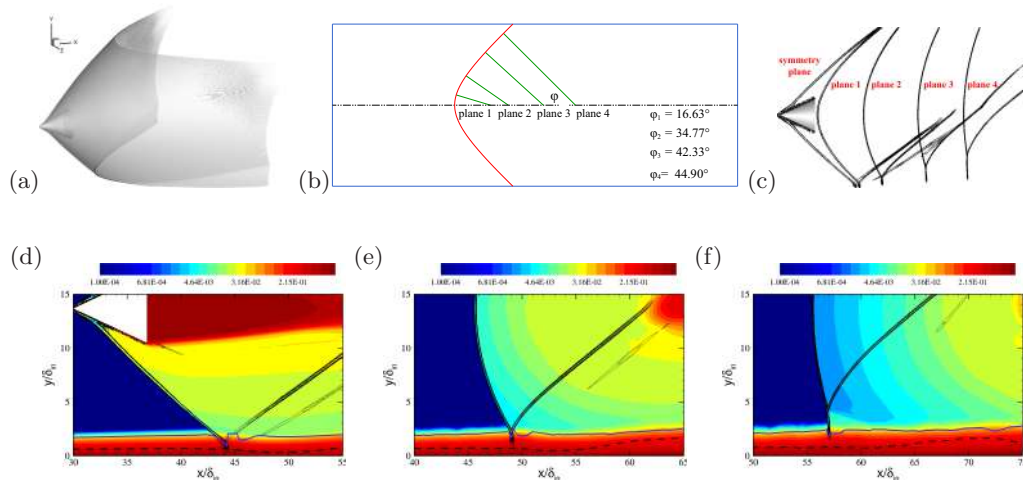
FIGURE 9. Analysis of shock structure: iso-surface of shock sensor (a); nomenclature for analysis in wall-normal planes (b); shock sensor in control planes (c); entropy contours in: symmetry plane (d), plane 2 (e), plane 3 (f). The blue solid line and the black dashed line in panels (d-f) represent, respectively, the boundary layer edge and the sonic line. Entropy levels are logarithmically spaced in the range $10^{-5} \leqslant s \leqslant 1.0$.
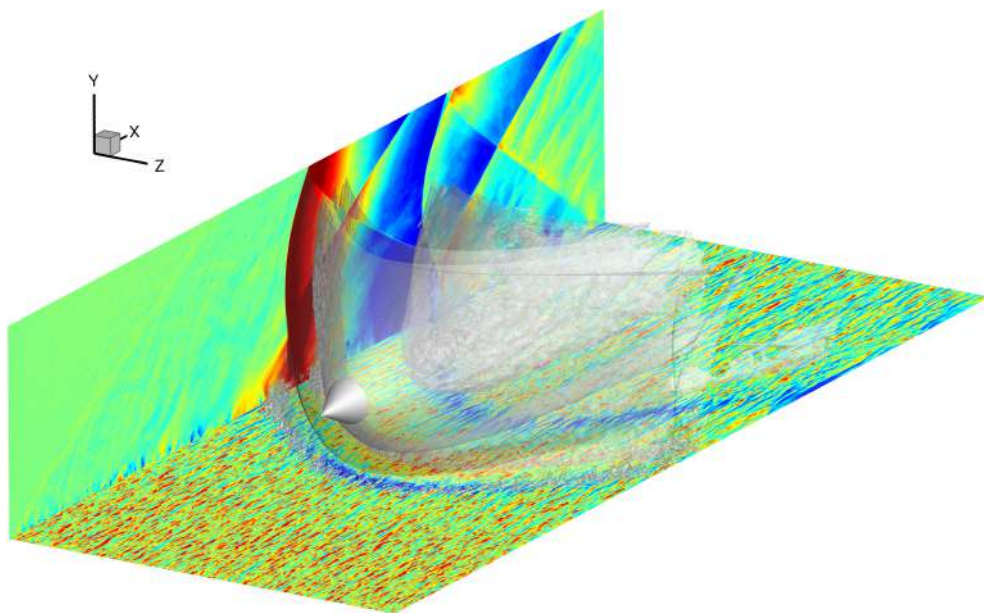

FIGURE 10. Three-dimensional view of CSBLI. The shock structure is educed through the pressure iso-surface $p = 1.1p_\infty$. Streamwise velocity contours are shown for $-0.3 < u/u_\infty < 2.3$ (color scale from blue to red) in a near-wall plane at $y^+ = 10.5$. Pressure contours are shown in a side plane for $0.8 < p/p_\infty < 1.2$ (color scale from blue to red). Supplementary movie 2 is available for this figure.

interacting shock. Streaks are found to reform quickly past the reflected shock, and they undergo a second suppression/reformation cycle across the second APG zone associated with wall impingement of the recompression shock.

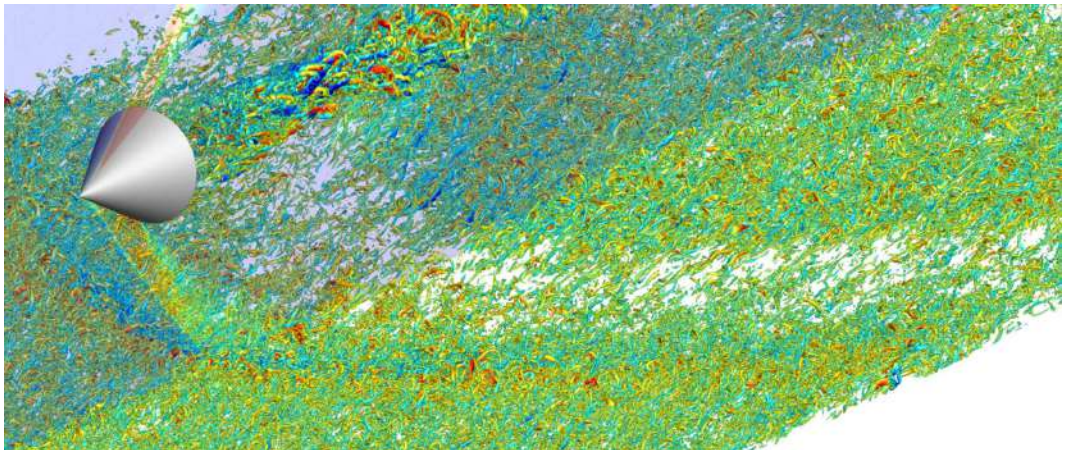Interaction of the boundary layer with a conical shock has a strong impact on the

FIGURE 11. Vortical structures in CSBLI. Vortices are educed through the iso-surface of the swirling strength ($\lambda_{ci} = 1.24u_\infty/\delta_{in}$), and colored with the wall-normal velocity ($-0.37 < v/u_\infty < 0.37$, color scale from blue to red). Supplementary movie 3 is available for this figure.

structure and number of vortical eddies populating the near-wall region. In figure 11 we report a three-dimensional rendering of vortical structures detected as iso-surfaces of the swirling strength, defined as the imaginary part of the complex conjugate eigenvalue of the velocity gradient tensor (Zhou *et al.* 1999). Visual inspection of many flow samples (supplementary movie 3) shows a vortex population in the ZPG region which is similar to what found in incompressible boundary layers (Wu & Moin 2009), including some hairpin-shaped vortices as well as more asymmetric, cane-shaped vortices. The vortices tend to disappear in the FPG region, and to reform past the recompression shock, but setting a lower threshold would still show weaker eddies in the expansion zone. Many hairpin-shaped vortices are also observed in the wake region past the shock generator, which propagate downstream evolving into ring-shaped eddies.

3.3. *Wall pressure*

An important feature in shock/boundary layer interactions is the steady and unsteady wall pressure load, which may have important impact on the behavior of the under-lying structural components. The mean wall pressure $\bar{p}_w$ across the interaction zone is compared in figure 12 with the experimental data of Hale (2015), obtained with pressure-sensitive paint. Good agreement is observed in the fore part of the pressure map, whereas differences are observed in the aft part, where the experiment exhibits a change of curvature of the iso-lines, which was attributed to side walls effects. In order to verify this speculation, two RANS simulations have been carried out at the same flow conditions as the experiment, one with the same spanwise domain as the experiment, and one with the same spanwise domain as the DNS (figures are omitted for brevity). Similar behavior of wall pressure as in the experiment was in fact observed in the small domain, whereas the same behavior as DNS was observed in the wider domain, which supports spanwise confinement as responsible for the observed differences.

Despite the described differences and the previously cited Reynolds number disparity, figure 12 shows nevertheless favourable comparison, at least limited to the experimental measurement window. This is better seen in figure 13, where we show mean pressure profiles at two spanwise locations. The figure well brings out the N-wave wall signature of the conical shock, with pressure rising sharply at the nominal shock impingement
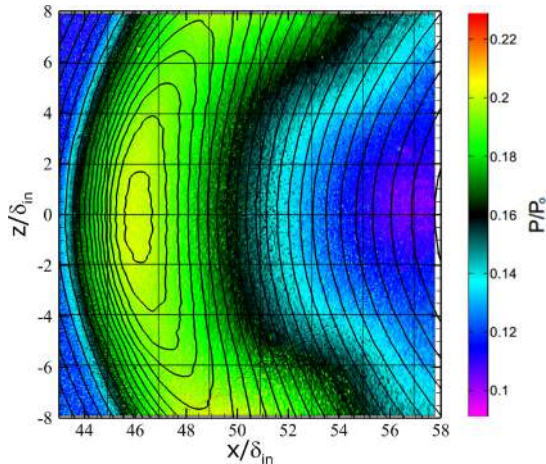
FIGURE 12. Mean wall pressure as obtained from experiments (Hale 2015, flooded contours) and from DNS (black lines). Contour levels are shown for $0.09 < p/p_0 < 0.23$, where p_0 is the free-stream total pressure.
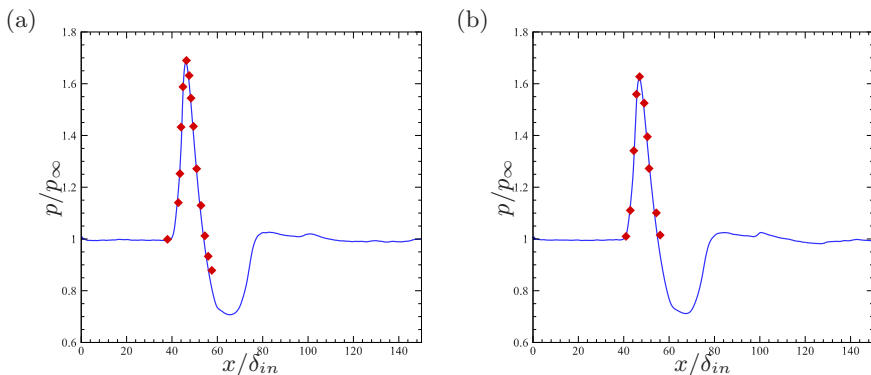

FIGURE 13. Mean wall pressure profiles at different spanwise positions: $z/\delta_{in} = 0$ (a); $z/\delta_{in} = 4.35$ (b). Lines, DNS; symbols, experiment (Hale 2015).

location, then decreasing almost linearly to a value which is lower than the free-stream, and increasing again upon impingement of the recompression shock. The peak value along the symmetry line is attained at approximately $x/\delta_{in} \approx 46$, whereas the peak is slightly shifted downstream at the other spanwise station, owing to the hyperbolic shape of the shock foot. After passing through the shock, pressure decreases upon passage of the expansion waves generated at the cone trailing edge. As flow develops downstream, pressure rises again in the second APG region ($x/\delta_{in} \approx 66$). Finally, the flow returns to a nearly ZPG condition. It should be noted that the same wall pressure pattern was observed in the experiments of Gai & Teh (2000).

Further comparison with experimental data are shown in figure 14, where the stream-wise velocity component and its root-mean-square are considered. The comparison of the mean velocity is quite favourable for $y/\delta_{in} \geqslant 0.2$, although largely different Reynolds numbers yield visibly different upstream influence, whereas PIV data for $y/\delta_{in} \leqslant 0.2$ is probably not reliable. Similar considerations also apply to u_{rms}, although differences are enhanced in the region of maximum turbulence intensity. Based on the comparison
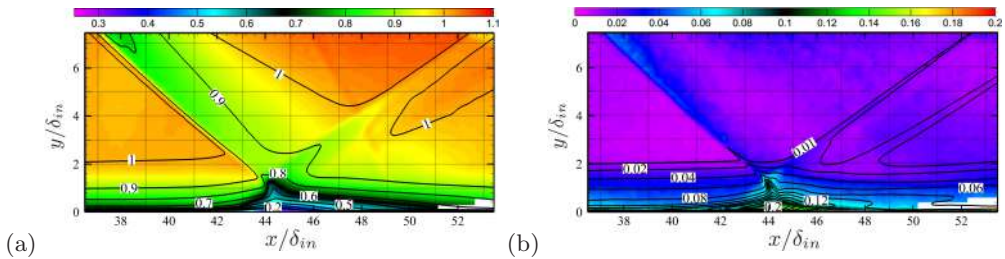
FIGURE 14. Mean streamwise velocity (a) and streamwise velocity r.m.s. (b): comparison between DNS (lines) and experiment (Hale 2015, flooded contours) Contours are shown for $0.2 < u/u_\infty < 1.1$, $0 < u_{rms}/u_\infty < 0.2$.
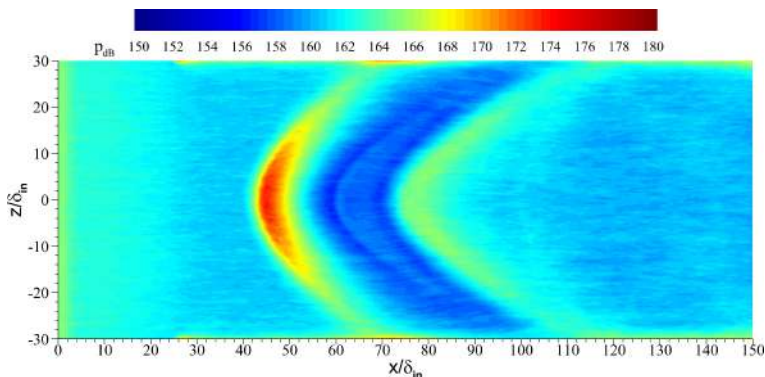

FIGURE 15. Contours of root-mean-square pressure fluctuations (p_{rms}) in the wall plane, in dB scale, $p_{dB} = 20 \log_{10}(p/2 \cdot 10^{-5} \text{Pa})$, assuming $p_\infty = 1\text{atm}$. Contour levels are shown from 150 to 180, from blue to red.

reported in the previous figures we can confidently conclude that the DNS results adequately reproduce the flow physics.

The root-mean-square pressure fluctuations contours are shown in figure 15. Strong spatial connection of this distribution is found with that of the vortical structures shown in figure 11. In particular, the largest values of p_{rms} are found at the interacting shock foot, especially around the symmetry axis where the shock is stronger. Consistent decrease of the fluctuating pressure loads is observed past the incident shock in the FPG region, which is depleted with eddies. A secondary peak is observed further downstream, corresponding to re-formation of the vortical structures. Numerical artifacts should be noted on the side boundaries, which are due to the imperfect nature of the numerical radiating boundary conditions, especially in the presence of waves not propagating orthogonally to the computational boundary. These effects are however confined to a narrow layer adjacent to the boundaries.

3.4. *Boundary layer development*

In order to characterize the spatial development of the wall boundary layer, we analyze the distributions of the displacement and momentum thicknesses, defined in equations (3.1), (3.2). The streamwise distributions of the displacement thickness (δ^*), of the momentum thickness (θ) and of the incompressible shape factor ($H_i = \delta_i^*/\theta_i$) along the symmetry plane are shown in figure 16(a). Upstream of the cone leading edge H_i varies between 1.55 and 1.75, as appropriate for canonical ZPG boundary layers at
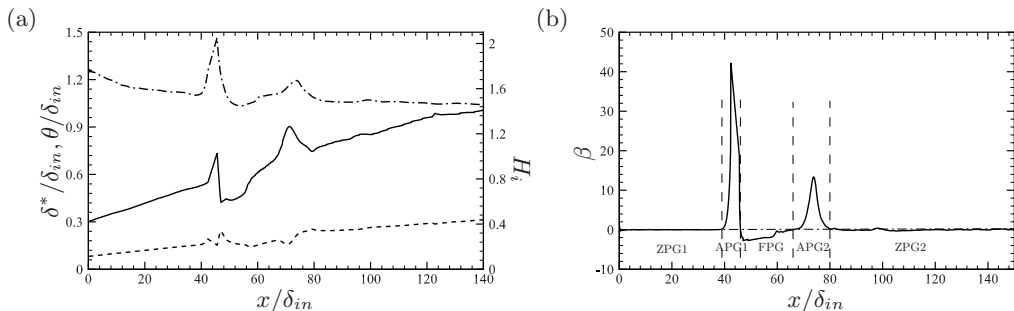
(a)

(b)

FIGURE 16. Streamwise evolution of boundary layer properties in the symmetry plane: (a) displacement thickness (solid), momentum thickness (dashed), shape factor (dash-dot); (b) Clauser pressure gradient parameter.
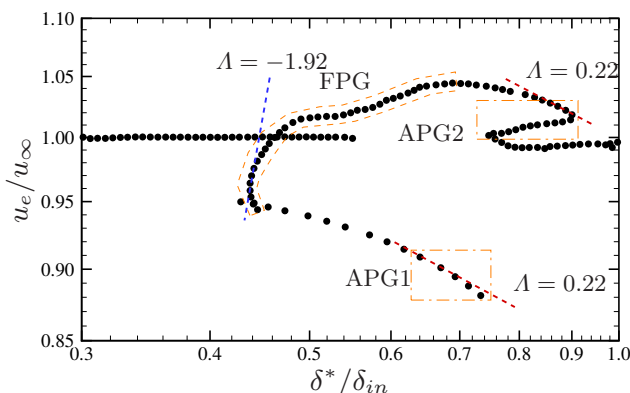

FIGURE 17. External velocity as a function of boundary layer displacement thickness along the symmetry plane. Dashed lines denote the power-law scalings given in equation (3.7).

low Reynolds number (Wu & Moin 2009). Corresponding to the leading edge of the interaction zone, the displacement thickness increases sharply, whereas the momentum thickness is relatively unaffected. Hence, the shape factor attains a maximum value $H_i \approx 2.0$, indicating a less full velocity profile. The displacement thickness undergoes a sudden drop in the FPG region followed by gradual recovery, and a new peak is observed in the second APG region, also corresponding to a peak of H_i. Past $x/\delta_{in} \approx 90$, the boundary layer recovers an equilibrium state which is an ideal continuation of the undisturbed upstream state.

Non-equilibrium states of boundary layers upon imposed pressure gradient are traditionally analyzed in terms of Clauser pressure gradient parameter, defined as (Clauser 1954)

$$\beta = \frac{\delta^*}{\rho_w u_\tau^2} \frac{\mathrm{d}\bar{p}_w}{\mathrm{d}x}, \qquad (3.5)$$

whose distribution along the symmetry axis is shown in figure 16(b). According to the DNS data, the flow field may be divided into five parts: ZPG1, the upstream ZPG region, with $\beta \approx 0$; APG1, the first APG region, where β exhibits a sharp positive peak; FPG, where β is negative as the flow accelerates; APG2, the second APG region, where β attains a second positive peak; ZPG2, the downstream ZPG region where equilibrium conditions are recovered.

Castillo & George (2001) proposed that the proper velocity scale for the outer part
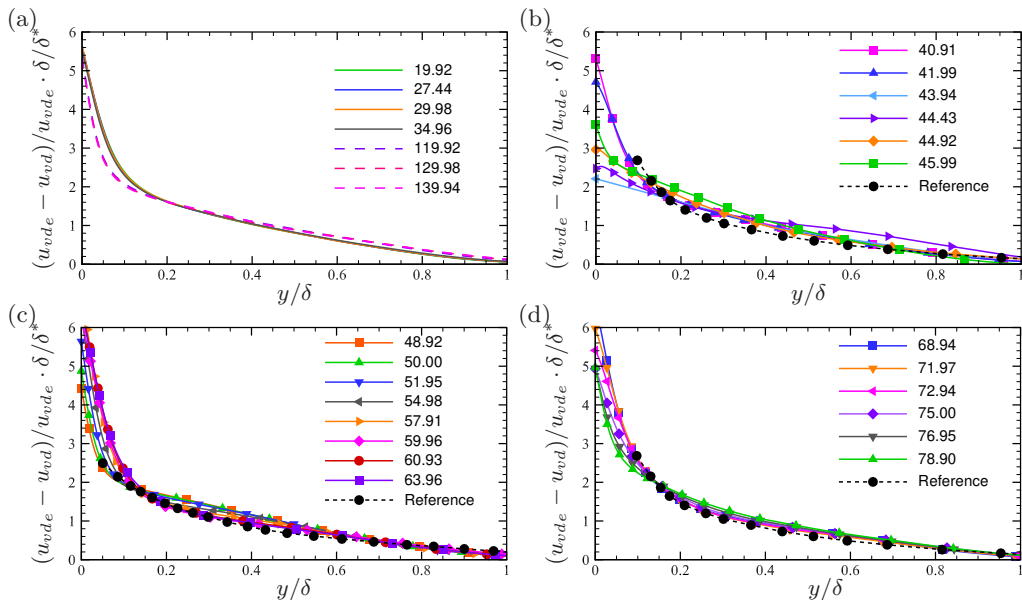
FIGURE 18. Mean velocity defect profiles at different streamwise stations in region ZPG1+ZPG2 (a), APG1 (b), FPG (c), APG2 (d). Reference data from Song & Eaton (2004) and Aubertine & Eaton (2005) are shown in panels (c) and (b, d), respectively.

of the boundary layer is the external velocity u_e rather than the friction velocity, and accordingly they introduced a modified pressure gradient parameter defined as

$$\Lambda = \frac{\delta}{\rho_e u_e^2 \mathrm{d}\delta/\mathrm{d}x} \frac{\mathrm{d}\bar{p}_w}{\mathrm{d}x} = -\frac{\delta}{u_e \mathrm{d}\delta/\mathrm{d}x} \frac{\mathrm{d}u_e}{\mathrm{d}x}, \qquad (3.6)$$

where δ is any measure of the boundary layer thickness. They suggested that, at least in the absence of mean flow separation, the admissible equilibrium states corresponding to self-similar velocity distributions must have constant value of Λ, which in turn implies power-law dependence of the boundary-layer thickness on the external velocity, namely

$$\delta \sim u_e^{-1/\Lambda}. \qquad (3.7)$$

It was found that most experimental data for boundary layers in adverse and favourable pressure gradient are in fact in equilibrium according to this definition, and three values of Λ were found to be possible: $\Lambda = 0.22$ in APG, $\Lambda = -1.92$ in FPG and $\Lambda = 0$ in ZPG. This is scrutinized in figure 17, where we show the boundary layer external velocity u_e (evaluated at $y = \delta_e$, as explained in §3.1) as a function of the boundary layer displacement thickness. The figure suggests very partial success of theoretical predictions, mainly limited to the APG regions, where scaling not far from the predicted $\Lambda = 0.22$ is observed, whereas the FPG region seems to have a behavior very different from the theoretical equilibrium state.

Self-similarity of the velocity profiles in the various zones is checked in figure 18, where we show the van Driest transformed velocity multiplied by δ/δ^* to remove effects of upstream conditions and local Reynolds number on the outer velocity profile (Zagarola & Smits 1998). In the ZPG1 and ZPG2 regions the velocity profiles do in fact collapse on a single curve, with the obvious exception of the near-wall region which suffers Reynolds number dependence. Similar considerations can be made for the FPG and the APG2 regions, which show a good degree of universality, and in which the defect
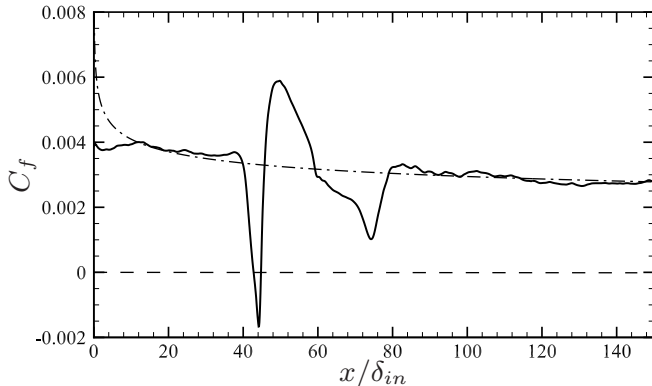
FIGURE 19. Mean friction coefficient in the symmetry plane. The dash-dotted line refers to equation (3.8).

velocity profiles well match reference experimental data for FPG flows (Song & Eaton 2004) and for APG flows (Aubertine & Eaton 2005). Not surprisingly, large deviations from a common distribution are observed in APG1 region, which experiences strong APG conditions and in which the flow even undergoes mean separation.

3.5. *Analysis of flow reversal*

The imposed adverse pressure gradient causes flow retardation along with locally reversed flow. The distribution of the mean friction coefficient $C_f = 2\tau_w/\rho_\infty u_\infty^2$, with $\tau_w = \mu_w(\partial \tilde{u}/\partial y)_w$ is shown in the symmetry plane in figure 19. Upstream of the interaction zone and in the downstream ZPG2 region the friction coefficient well follows the power-law behavior predicted by simple theory (Smits & Dussauge 2006), namely

$$C_f = k\,Re_x^{-1/7}, \tag{3.8}$$

with $k = 0.0192$, with the obvious exception of the inflow region where the boundary layer is not properly developed yet. Mean flow reversal in the symmetry plane is observed in the APG1 region, whereas C_f overshoots its upstream value in the FPG region right past the reattachment point. A secondary minimum of C_f is found in the APG2 region, where however the flow is not detached in mean sense.

Additional insight into the nature of wall flow reversal may be gained from figure 20, where we show the instantaneous wall friction and the statistical frequency of events with wall flow reversal (say $\overline{\gamma}$). Figure 20(a) shows that both the APG1 and APG2 regions feature a substantial fraction of flow reversal events, which are however scattered and interspersed with regions of attached flow. On the other hand, the FPG region is depleted with reverse flow events, and it features friction excess over the upstream value. The intermittency data are shown in panel (b). The data can be interpreted in light of the classification proposed by Simpson (1989), according to which incipient detachment occurs with instantaneous backflow 1% of the time; intermittent transitory detachment occurs with instantaneous backflow 20% of the time; transitory detachment (amounting to mean flow reversal) happens with 50% probability of instantaneous backflow. According to figure 20(b), mean flow reversal is found to occur only in the APG1 region around the symmetry line, whereas the flow becomes unidirectional in the mean away from the symmetry axis where pressure gradient is milder. Hence, the reversed flow region tends to become narrower along the z direction, eventually vanishing at $z \approx \pm 7.7\delta_{in}$. Transitory detachment is observed both in the APG1 and APG2 regions,
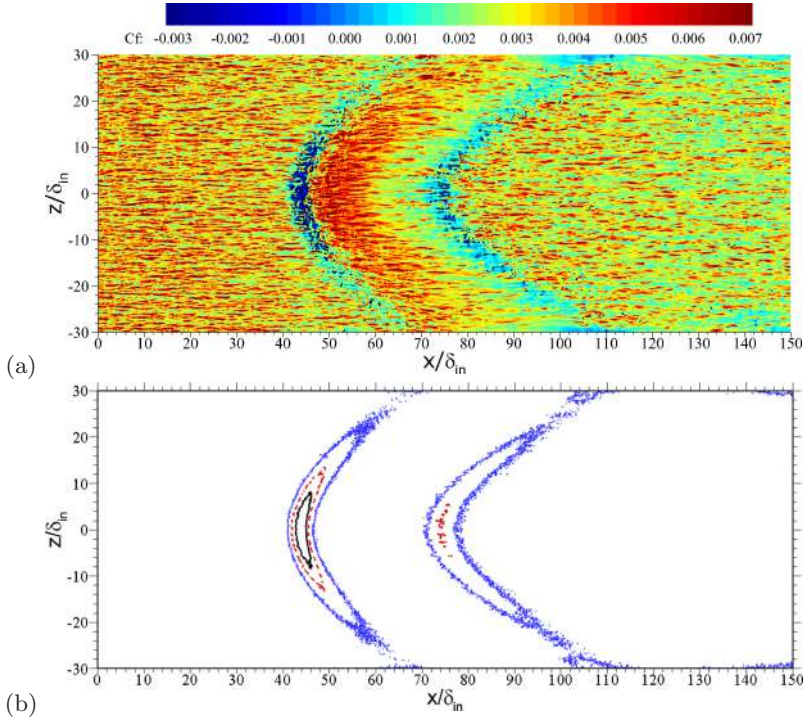
FIGURE 20. Instantaneous contours of wall friction (a) and of flow reversal probability $\overline{\gamma}$ (b) at the wall surface. The contour levels $\overline{\gamma} = 0.5$ (solid), 0.2 (dashed), 0.01 (dotted) are shown in panel (b).
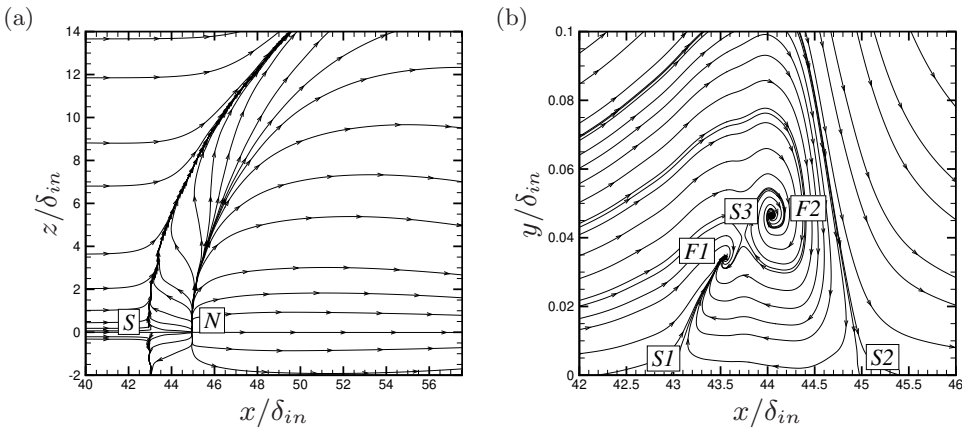

FIGURE 21. Limit wall streamlines of mean flow field (a), and streamtraces in the symmetry plane (b), highlighting critical points: N, nodes; S, saddle points; F, foci. Note that axes in panel (b) are not to scale.

to a much lesser extent in the latter case. Interestingly, an extended region with incipient detachment is observed in both APG zones, with no significant size difference.

The flow topology is further brought out from the analysis of the limit streamtraces in the wall plane and of the streamtraces in the symmetry plane, reported in figure 21. The wall limiting streamlines exhibit a pattern similar to that resulting from separation induced by an obstacle (Délery 2001), and the flow features a saddle point associated

with three-dimensional flow separation, which emanates from a line of coalescence (separation), and spirals into the vortical center (Dallmann 1983; Knight *et al.* 1987). Three-dimensionality of the flow also reflects in the streamlines shown in panel (b) being open, whereas the streamlines should be closed in two-dimensional steady flow. The flow past the line of coalescence is characterized by the presence of a node at $x/\delta_{in} \approx 45$ in the symmetry plane associated with a divergence line (attachment). The wall streamtraces are issued from the nodal point and partly converge into the coalescence line and partly are deflected downstream. This wall pattern is classically associated with the formation of a horseshoe vortex bending in the downstream direction, as is clarified in figure 21(b). A very similar organization was also recovered in the experiments of Gai & Teh (2000). Visualization in the symmetry plane highlights the presence of two saddle points at the wall (S1 and S2), being respectively the signature of the separation and reattachment point, and, according to the classification of Chong *et al.* (1990), two foci of stable type (F1 and F2), separated by a third saddle point (S3). This is to indicate that the horseshoe vortex is in fact split into two branches, which merge together moving away from the symmetry plane (not shown). It should be noted that the region of reversed flow, which may be defined as the region between the wall and the streamtrace entering saddle point S_2, is quite shallow, extending up to $y_R/\delta_{in} \approx 0.11$. Hence the aspect ratio of the separation bubble is very small, being $\mathit{\Re} = y_R/(x_{S_2} - x_{S_1}) \approx 0.057$, which is a typical value for turbulent separation bubbles, but much less than laminar ones (Kiya & Sasaki 1983).

3.6. *Turbulence statistics*

The structural modifications of boundary layer turbulence upon interaction with the conical shock are analyzed in this section. For that purpose, contours of the density-scaled velocity correlations $\overline{\rho}/\rho_w \widetilde{u_i'' u_j''}$ in the symmetry plane are shown in figure 22, upon normalization by the friction velocity at the upstream reference station, $u_{\tau ref}$. The figure supports general amplification of all turbulence intensities across the APG zones, however to a different extent. Specifically, the longitudinal velocity variance is amplified (with respect to its upstream value) by factor of about 2 through the APG1 zone, and by 1.6 in APG2. Similar amplifications are found for the wall-normal velocity correlation, whereas the spanwise velocity variance increases by a factor of 1.8 across APG1, and by a factor 1.1 in APG2. As expected, peaks of the normal turbulent stresses in the ZPG zones are found to lie closer to the wall for the streamwise component, and further away for the other components. To better highlight modifications of the turbulent stress tensor, in figure 22 we show the map of the Reynolds stress anisotropy function (Lumley 1978), defined as

$$F = 1 + 9II + 27III, \tag{3.9}$$

where II and III are the invariants of the anisotropy stress tensor, $b_{ij} = \tau_{ij}^*/\tau_{ii}^* - 1/3\delta_{ij}$, and which is a measure of the approach to either two-component turbulence (corresponding to $F = 0$) or a three-component isotropic state (corresponding to $F = 1$). Consistent with previous DNS data, figure 22 shows that in ZPG regions F is increasing from a nearly zero value at the wall where the flow is dominated by streaks, to a nearly uniform value of about 0.6 in the outer part of the boundary layer. As the flow crosses the interacting shock in the APG1 region the anisotropy indicator increases at any given y, indicating approach of turbulence to an isotropic state. The opposite effect is observed in the FPG region which shows consistent decrease of this indicator, accompanied by the previously noted re-formation of the streaks, and again increase is observed in APG2 region, prior to relaxation to an equilibrium state.
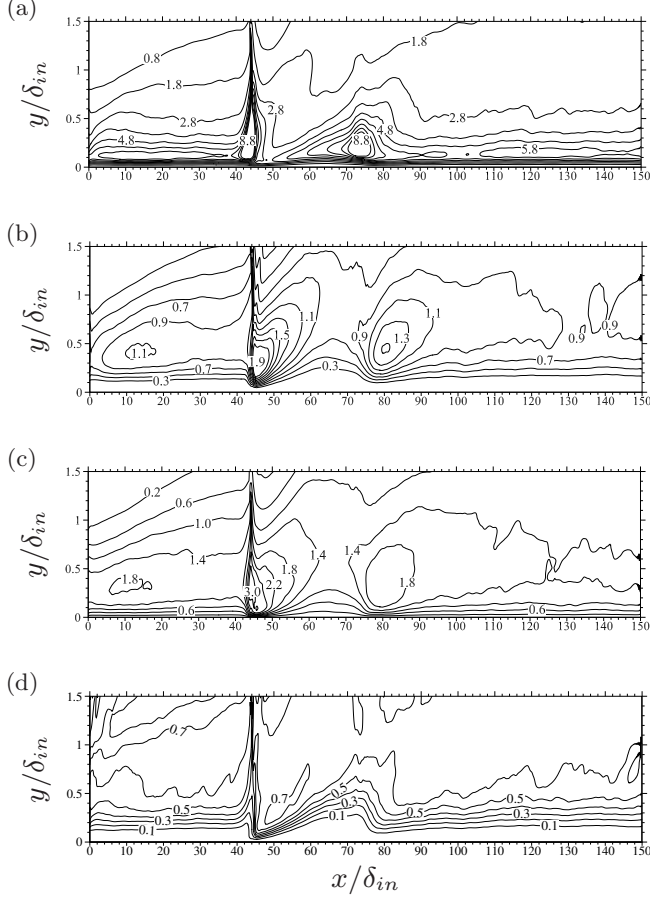
FIGURE 22. Maps of density-scaled turbulence intensities $(\overline{\rho}/\rho_w \widetilde{u_i''^2})$ in the symmetry plane, normalized by friction velocity at the upstream reference station (a, $i = 1$; b, $i = 2$; c, $i = 3$) and anisotropy indicator (d), as defined in equation (3.9).

The DNS database herein developed can be profitably exploited for testing hypotheses and checking predictions of turbulence closures. In the following, we explore predictive power and limitations of Boussinesq hypothesis, which postulates linear relationship between anisotropic turbulent stress tensor and mean strain tensor through a scalar eddy viscosity μ_T,

$$- \overline{\rho u_i'' u_j''} = 2\mu_T \tilde{S}_{ij}^* - \frac{2}{3}\overline{\rho}\kappa\delta_{ij}, \quad \tilde{S}_{ij}^* = \frac{1}{2}\left(\frac{\partial \tilde{u}_i}{\partial x_j} + \frac{\partial \tilde{u}_j}{\partial x_i}\right) - \frac{1}{3}\frac{\partial \tilde{u}_k}{\partial x_k}\delta_{ij}. \quad (3.10)$$

with $\kappa = 1/2\widetilde{u_k'' u_k''}$ the turbulence kinetic energy. An effective eddy viscosity can be extracted from DNS through contraction

$$\mu_T = -\frac{\left(\overline{\rho u_i'' u_j''} - \frac{2}{3}\overline{\rho}\kappa\delta_{ij}\right)\tilde{S}_{ij}^*}{2\tilde{S}_{ij}^* \tilde{S}_{ij}^*}. \quad (3.11)$$

This is compared in figure 23 with the the eddy viscosity obtained with RANS based on the Spalart-Allmaras one-equation model (Spalart & Allmaras 1992) in its classical form, without use of any compressibility correction. Good qualitative agreement is observed
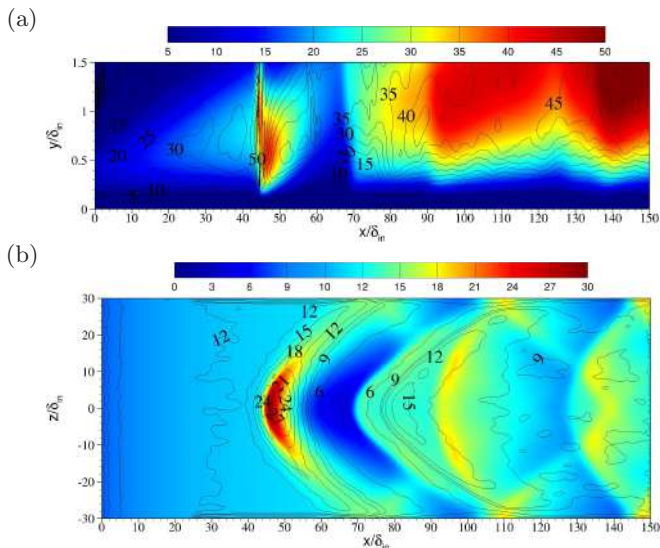
(a)

(b)

FIGURE 23. Eddy viscosity normalized by free-stream molecular viscosity (μ_T/μ_∞) in the symmetry plane (a) and in the plane $y = 0.25\delta_{in}$, as obtained from DNS (lines) and from RANS with Spalart-Allmaras model (flooded contours).

both in the symmetry plane and in a representative wall-parallel plane, with the eddy viscosity increasing in APG zones and decreasing in FPG zones and moving away from the symmetry plane. Quantitative differences are obviously present, and RANS is found to generally underestimate μ_T, especially upstream of the interaction, whereas the agreement improves downstream of the incident shock, owing to the previously noted flow isotropization. Additional discrepancies are due to the different prediction of the trailing shock position, which is further upstream in RANS owing to incorrect prediction of the recirculation extent past the shock-generating cone. It should also be noted that DNS tends to yield two distinct peaks in the region of maximum μ_T, whereas RANS predicts a single peak.

We now proceed to compare the computed Reynolds stress distributions with those modeled using the Boussinesq closure, with μ_T either determined after equation (3.11), or as predicted from RANS. The analysis is here limited to the off-diagonal Reynolds stress components, as the diagonal stresses are known to be poorly predicted by any linear eddy-viscosity model (Speziale 1987), which is also the case here. As seen in figure 24, the primary shear stress $-\overline{\rho u'' v''}$, is recovered with excellent accuracy when the 'exact' μ_T (3.11) is used, which is not unexpected as the other off-diagonal stresses are zero at the symmetry plane, and diagonal terms only contribute where anisotropy is significant. Good prediction is also achieved by RANS, with the previously noted differences in the vicinity of the trailing shock. This observation supports the generally acknowledged effectiveness of classical RANS for unidirectionally sheared flows.

Additional information related to the multi-dimensional character of turbulence in CSBLI may be gained by inspecting turbulent stresses in a wall-parallel plane, as shown in figure 25. Note that, for obvious symmetry reasons, only half of the full domain span is shown. The primary shear stress $-\overline{\rho u'' v''}$ shows two main peaks, corresponding to the APG zones, whose intensity decreases moving away from the symmetry plane. As previously observed in figure 24 for the symmetry plane, Boussinesq hypothesis works quite well for this component of the turbulent stress. Similar spatial organization is also
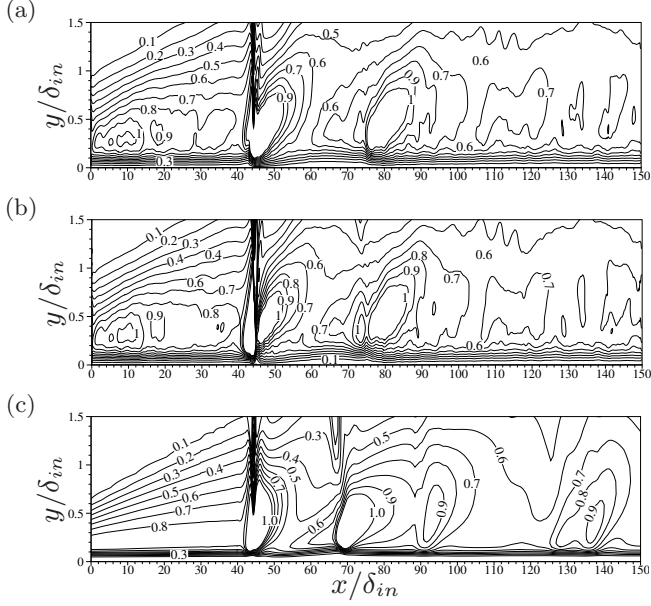
FIGURE 24. Maps of density-scaled primary turbulent shear stress $(-\overline{\rho}/\rho_w \widetilde{u''v''})$ in the symmetry plane, normalized by friction velocity at the upstream reference station, as obtained from DNS (a), from eddy-viscosity hypothesis (b) and from RANS (c).
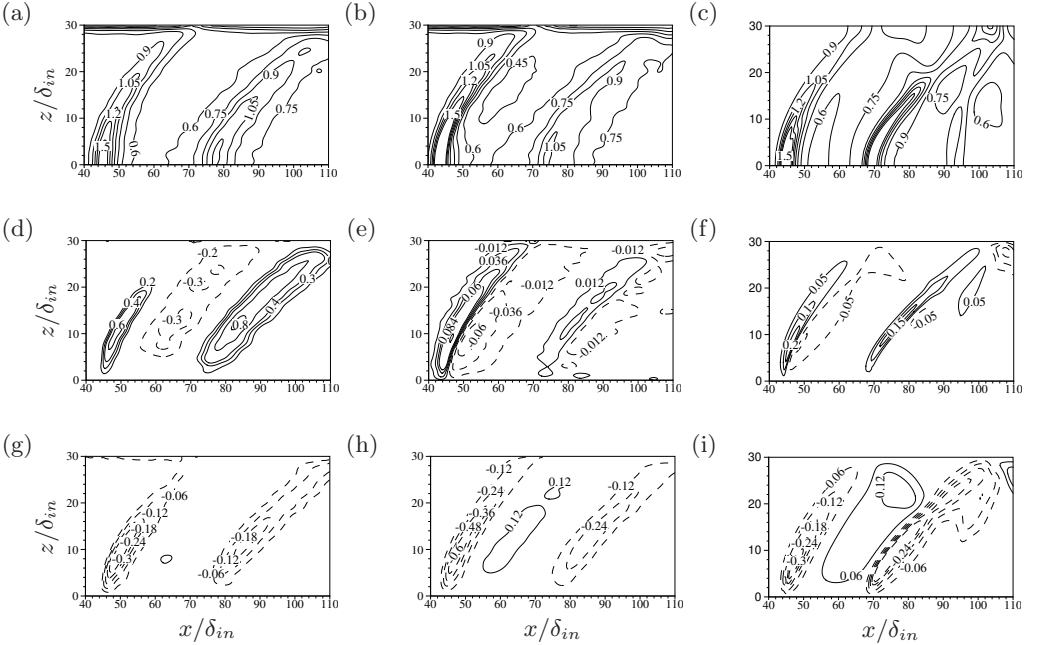

FIGURE 25. Maps of density-scaled turbulent shear stresses in wall-parallel plane $(y = 0.25\delta_{in})$, normalized by friction velocity at the upstream reference station, as obtained from DNS (a, d, g), with μ_T determined from equation (3.11) (b, e, h) and from RANS (c, f, i). (a, b, c) $-\overline{\rho}/\rho_w \widetilde{u''v''}$, (d, e, f) $-\overline{\rho}/\rho_w \widetilde{u''w''}$, (g, h, i) $-\overline{\rho}/\rho_w \widetilde{v''w''}$. Dashed lines denote negative values.

observed for the secondary shear stresses $-\overline{\rho u'' w''}$, $-\overline{\rho v'' w''}$, which become similar in magnitude away from the symmetry plane. However, whereas the primary shear stress is everywhere positive, the secondary stresses exhibit a change of sign from the APG to the FPG regions. As shown in the figure, this sign variation is well captured from the simple Boussinesq closure (middle column), thus showing that the secondary shear stresses are closely related to the respective mean velocity gradients. However, it should be noted that the numerical values are underestimated by a factor of about five in the case of $-\overline{\rho u'' w''}$, and generally overestimated in the case of $-\overline{\rho v'' w''}$, even when the 'exact' eddy viscosity is used. Similar results are obtained with RANS (right column). Hence, we conclude that Boussinesq hypothesis is still meaningful in this complex flow, although different eddy viscosities should be used for each stress component to fully exploit its potential. Possible improvements to Boussinesq approximation were applied to canonical geometrically two-dimensional SBLI by Gerolymos *et al.* (2004); Emory *et al.* (2011), whose predictive capabilities might be tested in this more challenging case.

4. Conclusions

The interaction of a conical shock wave with a turbulent boundary layer at free-stream Mach number $M_\infty = 2.05$, half-cone angle $\theta_c = 25°$ and Reynolds number $Re_\theta \approx 630$ has been analysed by means of DNS of the compressible Navier-Stokes equations. Detailed flow statistics have been presented, including mean flow properties and turbulent fluctuations. Particular effort has been made to characterize the geometry of the shock system and the three-dimensional features of the interaction region.

Consistent with experimental observations, the mean flow pattern is found to include a main conical shock which imposes a hyperbolic footprint on the underlying flat plate, and which causes thickening and local separation of the developing boundary layer. The incident shock is reflected as two conical shock waves, one arising because of the upstream influence mechanisms, and the second past the boundary layer reattachment. As theoretically predicted, analysis of the entropy fields obtained from DNS allows to discern transition from regular to Mach reflection with a distinct shock stem moving away from the symmetry plane, although the transition point is probably much farther than suggested by the inviscid theory. The compression waves originating within the cone wake also tend to coalesce to form a secondary weaker conical shock, which interacts with the boundary layer further downstream. Overall, this wave pattern imparts a distinctive N-wave signature at the wall, with a primary APG region followed by a FPG region, which is then closed by a secondary APG region bringing the boundary layer back to an equilibrium state. Very good agreement of the computed wall pressure signature is found with respect to reference experimental measurements.

The imposed wall pressure gradient is responsible for strong turbulence non-equilibrium in the boundary layer. In this respect, flow visualizations in the upstream ZPG region show that the outer part of the boundary layer is populated by hairpin-shaped vortices as well as more asymmetric, cane-shaped vortices. Vortices tend to disappear in the FPG region, and to reform past the recompression shock. Correspondingly, the near-wall streaks of high- and low-speed fluid which are present in the incoming ZPG region, are suppressed in the APG regions, to quickly reform downstream. Statistical analysis of flow reversal zones highlights mean flow separation in the primary APG zone accompanied with formation of a horseshoe vortex, whereas the secondary APG zone is characterized by intermittent detachment with scattered spots of instantaneous flow reversal.

¿From a quantitative standpoint we find that turbulence non-equilibrium is only partially captured by existing theoretical frameworks. In particular, we find that self-

similarity proposed by Castillo & George (2001) is partly attained in APG zones, whereas large departures are found in the FPG zone. Different amplification of the Reynolds stress components is observed in the APG regions, accompanied by a change in the geometry of the Reynolds stress tensor. Specifically, isotropy is favoured in APG regions, whereas an anisotropic two-component state is recovered in the FPG zone, associated with reformation of the streaks. The DNS database has been exploited to verify the validity of fundamental assumptions made in RANS turbulence closures based on Boussinesq hypothesis. In this respect, we find that the assumed proportionality between turbulent shear stress and related mean velocity gradient applies also when three-dimensionality effects are important, only the primary shear stress is predicted with reasonable accuracy, thus suggesting that tensor eddy viscosity models or full Reynolds stress closures might provide improved prediction. Future studies will be devoted to enlarging the DNS database by also including cases with stronger shocks and/or cone opening angles, and to further characterize the unsteady wall signature.

REFERENCES

Adams, N. A. 2000 Direct simulation of the turbulent boundary layer along a compression ramp at $M = 3$ and $Re_\theta = 1685$. *J. Fluid Mech.* **420**, 47–83.

Aubard, G., Gloerfelt, X. & Robinet, J. C. 2013 Large-eddy simulation of broadband unsteadiness in a shock/boundary-layer interaction. *AIAA J.* **51** (10), 2395–2409.

Aubertine, C. D. & Eaton, J. K. 2005 Turbulence development in a non-equilibrium turbulent boundary layer with mild adverse pressure gradient. *J. Fluid Mech.* **532**, 345–364.

Babinsky, H. & Harvey, J. K. 2011 *Shock wave-boundary-layer interactions*. Cambridge Univ. Press.

Bernardini, M., Modesti, D. & Pirozzoli, S. 2016 On the suitability of the immersed boundary method for the simulation of high-Reynolds-number separated turbulent flows. *Comput. Fluids* **130**, 84–93.

Castillo, L. & George, W. K. 2001 Similarity analysis for turbulent boundary layer with pressure gradient: outer flow. *AIAA J.* **39** (1), 41–47.

Chong, Min S, Perry, Anthony E & Cantwell, Brian J 1990 A general classification of three-dimensional flow fields. *Physics of Fluids A: Fluid Dynamics* **2** (5), 765–777.

Clauser, F. H. 1954 Turbulent boundary layers in adverse pressure gradients. *J. Aeronaut. Sci.* **21** (2), 91–108.

Dallmann, Uve 1983 Topological structures of three-dimensional vortex flow separation. In *16th Fluid and Plasmadynamics Conference*, p. 1735.

DeBonis, J. R., Oberkampf, W. L., Wolf, R. T., Orkwis, P. D., Turner, M. G., Babinsky, H. & Benek, J. A. 2012 Assessment of computational fluid dynamics and experimental data for shock boundary-layer interactions. *AIAA J.* **50** (4), 891–903.

Délery, J.M. 2001 Robert Legendre and Henry Werlé: toward the elucidation of three-dimensional separation. *Annu. Rev. Fluid Mech.* **33**, 129–154.

Délery., J.M. & Dussauge, J. P. 2009 Some physical aspects of shock wave/boundary layer interactions. *Shock Waves* **19** (6), 453–468.

Dolling, D. S. 2001 Fifty years of shock-wave/boundary-layer interaction research: what next? *AIAA J.* **39** (8), 1517–1531.

Dupont, P., Haddad, C. & Debieve, J. F. 2006 Space and time organization in a shock-induced separated boundary layer. *J. Fluid Mech.* **559**, 255–277.

Emory, M., Pecnik, R. & Iaccarino, G. 2011 Modeling structural uncertainties in Reynolds-averaged computations of shock/boundary layer interactions. *49th AIAA Aerospace*

Sciences Meeting including the New Horizons Forum and Aerospace Exposition 2011-479.
American Institute of Aeronautics and Astronautics.

FADLUN, E. A., VERZICCO, R., ORLANDI, P. & MOHD-YUSOF, J. 2000 Combined immersed-boundary finite-difference methods for three-dimensional complex flow simulations. *J. Comput. Phys.* **161** (1), 35–60.

GAI, S. L. & TEH, S. L. 2000 Interaction between a conical shock wave and a plane turbulent boundary layer. *AIAA J.* **38** (5), 804–811.

GEROLYMOS, G.A., SAURET, E. & VALLET, I. 2004 Oblique-shock-wave/boundary-layer interaction using near-wall Reynolds-stress models. *AIAA J.* **42**, 1089–1100.

HADJADJ, A. 2012 Large-Eddy Simulation of Shock/Boundary-Layer Interaction. *AIAA J.* **50** (12), 2919–2927.

HALE, J. 2015 Interaction between a conical shock wave and a plane compressible turbulent boundary layer at Mach 2.05. PhD thesis, UIUC.

HERRIN, JL & DUTTON, JC 1994 Supersonic base flow experiments in the near wake of a cylindrical afterbody. *AIAA J.* **32** (1), 77–83.

KIYA, M. & SASAKI, K. 1983 Structure of a turbulent separation bubble. *J. Fluid. Mech.* **137**, 83–113.

KNIGHT, DOYLE D, HORSTMAN, C, BOGDONOFF, SEYMOUR & SHAPEY, BRIAN 1987 Structure of supersonic turbulent flow past a sharp fin. *AIAA J.* **25** (10), 1331–1337.

LUMLEY, J.L. 1978 Computational modeling of turbulent flows. *Adv. Appl. Mech.* **18**, 123–176.

MIGOTSKY, E. & MORKOVIN, M. V. 1951 Three-Dimensional Shock-Wave Reflections. *J. Aeronaut. Sci.* **18** (7), 484–489.

MORGAN, B., DURAISAMY, K., NGUYEN, N., KAWAI, S. & LELE, S. K. 2013 Flow physics and RANS modelling of oblique shock/turbulent boundary layer interaction. *J. Fluid Mech.* **729**, 231–284.

O'ROURKE, J. 1998 *Computational geometry in C*. Cambridge Univ. Press.

PANOV, Y. A. 1968 Interaction of incident three-dimensional shock with a turbulent boundary layer. *Fluid Dynam.* **3** (3), 108–110.

PIROZZOLI, S. 2010 Generalized conservative approximations of split convective derivative operators. *J. Comput. Phys.* **229** (19), 7180–7190.

PIROZZOLI, S. 2011 Numerical methods for high-speed flows. *Annu. Rev. Fluid Mech.* **43**, 163–194.

PIROZZOLI, S. & BERNARDINI, M. 2011a Direct numerical simulation database for impinging shock wave/turbulent boundary-layer interaction. *AIAA J.* **49** (6), 1307–1312.

PIROZZOLI, S. & BERNARDINI, M. 2011b Turbulence in supersonic boundary layers at moderate Reynolds number. *J. Fluid Mech.* **688**, 120–168.

PIROZZOLI, S., BERNARDINI, M. & GRASSO, F. 2010 Direct numerical simulation of transonic shock/boundary layer interaction under conditions of incipient separation. *J. Fluid Mech.* **657**, 361–393.

PIROZZOLI, S. & GRASSO, F. 2006 Direct numerical simulation of impinging shock wave/turbulent boundary layer interaction at $M = 2.25$. *Phys. Fluids* **18** (6).

POINSOT, T. J. & LELE, S. K. 1992 Boundary conditions for direct simulations of compressible viscous flows. *J. Comput. Phys.* **101** (1), 104–129.

SIMPSON, R. L. 1989 Turbulent boundary-layer separation. *Annu. Rev. Fluid Mech.* **21** (1), 205–232.

SMITS, A. J. & DUSSAUGE, J. P. 2006 *Turbulent shear layers in supersonic flow*. Springer Science & Business Media.

SONG, S. & EATON, J. K. 2004 Reynolds number effects on a turbulent boundary layer with separation, reattachment, and recovery. *Exp. Fluids* **36** (2), 246–258.

SPALART, P. & ALLMARAS, S. 1992 A one-equation turbulence model for aerodynamic flows. In *30th Aerospace Sciences Meeting and Exhibit*. American Institute of Aeronautics and Astronautics.

SPEZIALE, C. G. 1987 On nonlinear k-l and k-ϵ models of turbulence. *J. Fluid Mech.* **178**, 459–475.

SZIROCZAK, D. & SMITH, H. 2016 A review of design issues specific to hypersonic flight vehicles. *Prog. Aerosp. Sci.* **84**, 1–28.

TESSICINI, F., IACCARINO, G., FATICA, M., WANG, M. & VERZICCO, R. 2002 Wall modeling

for large-eddy simulation using an immersed boundary method. *CTR Annu. Res. Briefs, Stanford, CA* pp. 181–187.

TOUBER, E. & SANDHAM, N. D. 2011 Low-order stochastic modelling of low-frequency motions in reflected shock-wave/boundary-layer interactions. *J. Fluid Mech.* **671**, 417–465.

WU, X. & MOIN, P. 2009 Direct numerical simulation of turbulence in a nominally zero-pressure-gradient flat-plate boundary layer. *J. Fluid Mech.* **630**, 5–41.

XU, S. & MARTIN, M. P. 2004 Assessment of inflow boundary conditions for compressible turbulent boundary layers. *Phys. Fluids* **16** (7), 2623–2639.

ZAGAROLA, M. V. & SMITS, A. J. 1998 Mean-flow scaling of turbulent pipe flow. *J. Fluid Mech.* **373**, 33–79.

ZHOU, J., ADRIAN, R. J., BALACHANDAR, S. & KENDALL, T. M. 1999 Mechanisms for generating coherent packets of hairpin vortices in channel flow. *J. Fluid Mech.* **387**, 353–396.

ZUO, F. & HUANG, G. 2018 Numerical investigation of bleeding control method on section-controllable wavecatcher intakes. *Acta Astronaut.* **151**, 572–584.

ZUO, F., HUANG, G. & XIA, C. 2016 Investigation of internal-waverider-inlet flow pattern integrated with variable-geometry for TBCC. *Aerosp. Sci. Technol.* **59**, 69–77.